

Graphene-Modified Glassy Carbon Electrodes: Correlations between Electrochemical Performance, Film Morphology and Composition

Paula M. V. Fernandes, Carlos M. Pereira, José M. Campiña*, A. Fernando Silva

Centre for Research in Chemistry of The University of Porto (CIQUP), Dept. of Chemistry and Biochemistry, Faculty of Sciences, Rua do Campo Alegre 687, 4169-007 Porto, Portugal

*E-mail: jpina@fc.up.pt

Received: 9 November 2021 / Accepted: 17 December 2021 / Published: 2 February 2022

Graphene and its derivatives are generally portrayed as electron transfer enhancers that effectively boost the electrochemical response of classic electrodes for applications in renewable energy, electronics, or analysis (amongst others). However, a number of fundamental studies have challenged this view. In certain reports, not only could no beneficial effect be demonstrated, but the opposite was concluded. If we want to advance towards a more rational design of high-performance electrode devices, these discrepancies need to be cleared and the fundamental aspects of electron transfer reactions through graphene-electrodes further understood. The present study contributes to this cause by exploring the relationships between the structure and morphological appearance of graphene films and their electrochemical performance in fundamental proof-of-concept experiments. The results unveil that important differences in the structure and morphology of the films (which are tightly related to the composition and load of graphene materials) govern the electrochemical response of the modified electrodes. Thereby, a possible explanation for the apparently contradictory conclusions reported in the literature is provided.

Keywords: electrode modification, thin films and coatings, electron transfer studies, graphene oxide, reduced graphene oxide

1. INTRODUCTION

Altering the chemical composition and structure of pristine graphene (a one-atom-thick flat mesh of carbon isolated for the first time in 2004 [1]) can negatively impact some of its outstanding physical properties [2,3]. However, these also represent an amazing opportunity to endow new chemistries for covalent/electrostatic modification, enhanced electrocatalytic properties [4], improved charge carrier densities, or to open a bandgap [5]. The potential of electrode modification with graphene-based nanomaterials (GNMs) in analysis, catalysis, or renewable energy, was soon

recognized [6-12]. In these devices, GNMs often play a double role as an electrical transducer (providing enhanced electron conductivity & electron transfer, ET, rates) and a compatible substrate for the deposition of proteins, aptamers, NPs, polymers, and so on. While single-layer graphene prepared by chemical vapor deposition (CVD-SLG) has been typically applied in field-effect transistors [6], electrochemical applications have relied more on graphene obtained through liquid exfoliation routes (LEG).

LEGs bring advantages like lower fabrication costs, scalable production, solution processing, and the absence of transfer steps. However, these gains come at the expense of degraded electrical and thermal conductivities, more defective structures, frequent doping with heteroatoms, and the possible formation of few-layer graphene flakes (FLG). As an extreme case, graphene oxide (GO; a water-soluble derivative functionalized with vast amounts of oxygen-containing groups) behaves like an electrical insulator. Many attempts to restore sp^2 hybridization at GO have been described [13-15], but none has accomplished its complete reduction. Moreover, the resulting reduced GO (rGO) can be regarded as a more exciting electrode material due to the combination of partially-restored electrical conductivity and their remaining electrocatalytic properties [16,17]. Notwithstanding that it is generally claimed that GNM-modified electrodes exhibit enhanced electrochemical performances, this view has been challenged in some pivotal studies [6,18]. For example, Pumera et al. showed that neither SLG nor FLG were able to improve the sensitivity to uric acid detection achieved by a graphite microparticle-modified electrode [19].

Different studies have also established that ET processes through peripheral edge-plane and edge-like basal defects (more abundant in LEGs) are significantly faster than those across “pristine” basal domains (which can be envisioned as relatively inert) [20-22]. In the same line, Brownson et al. demonstrated slow ET kinetics for electrodes modified with CVD-SLGs (because of their high basal-to-edge site ratio) [18] and Chekin et al. presented improvements in the electrochemical response of glassy carbon electrode (GCE) modified with rGO, porous rGO (p-rGO), and N-doped p-rGO, (compared to that coated with CVD-SLG) [23]. The interplay between the coating methodologies and the microstructure of the film must be one of the keys to understanding and predicting the response of the electrodes (since it determines relevant aspects such as surface coverage, electroactive area, thickness, porosity, etc). Additional difficulties may also arise from the lack of control on the orientation of the sheets/flakes to form well-ordered macroscopic domains.

To get deeper insights into the fundamental aspects governing the assembly and ET properties of GNM-electrodes, this work investigates the structure of ultrathin films of commercial GO and rGO deposited onto GCE under different conditions. Then, this information is compared with the electrochemical response registered for the modified electrodes in the presence of a reversible redox couple. The films were characterized with attenuated total reflectance Fourier transform infrared spectroscopy (ATR-FTIR), X-ray photoelectron spectroscopy (XPS), atomic force microscopy (AFM), field-effect scanning electron microscopy (FESEM), energy-dispersive X-ray analysis (EDX), cyclic voltammetry (CV), and electrochemical impedance spectroscopy (EIS). The results confirmed the tight correlation between the architecture of the coatings and the particularities of the redox response.

2. EXPERIMENTAL

2.1 Materials

GO (O%: 41-50) and rGO (O%: 13-17%) powders were purchased to Graphenea (San Sebastián, Spain) together with a 0.5 mg·mL⁻¹ water dispersion of GO (>95% monolayer content; O%: 14-50). Disodium hydrogen phosphate dihydrate (>98%), potassium dihydrogen phosphate (>98%), NaCl (>99%), and glacial acetic acid (≥99.8%) from Sigma Aldrich; potassium hexacyanoferrate(II) trihydrate (p.a., K₄[Fe(CN)₆]·3H₂O) and potassium hexacyanoferrate(III) (p.a.; K₃[Fe(CN)₆]) from Fluka; sodium acetate trihydrate (suprapur) from Merck; ethanol (96% vol.) from Aga; and N₂ (N45) from Air Liquide; were used without further purification. Solutions and buffers were prepared in ultrapure water (UPW) from a Milli-RO3 Plus system (resistivity: 18.2 MΩ·cm) and stored at 4 °C.

2.2 Methods

Electrochemical experiments were carried out at room temperature (RT) in a three-electrode cell. GCE and a couple of Pt and Ag wires served as working, auxiliary, and pseudo-reference electrodes, respectively. Wires were flame-annealed and subsequently washed in abundant UPW. 0.05 M phosphate-buffered saline (PBS; 150 mM NaCl; pH=7.4; aka electrolyte A) and the same medium plus 2 mM [Fe(CN)₆]^{3-/4-} (electrolyte B) were purged with N₂ for 10 min before measurements. CVs were recorded with a Voltalab PGZ301 potentiostat (Radiometer Analytical) in the potential windows of -0.8//+0.8 V (electrolyte A) and -0.3//+0.6 V (electrolyte B). Unless otherwise stated, the scan rate (ν) was 0.05 V·s⁻¹. The half-wave potential ($E_{1/2}$) measured from the CVs was ≈+0.15 V in all cases. Diffusion coefficients, D (cm²·s⁻¹), were calculated using the Randles-Sevcik equation at 298 K:

$$j_p = 2.69 \cdot 10^5 \cdot D^{1/2} \cdot n^{3/2} \cdot C \cdot \nu^{1/2} \quad (1)$$

where C is the bulk concentration of the probes (2·10⁻⁶ mol·cm³) and the number of electrons transferred was considered $n=1$. ν was swept in the range 0.001-0.2 V·s⁻¹ and the peak current densities (anodic, j_{PA} , and cathodic, j_{PC}) were read from the corresponding CVs. Impedance spectra were taken using the same setup. To this end, sinusoidal waves of 10 mV oscillation amplitude (OA) and frequency ranging from $\omega=10^4$ to 10⁻¹ Hz were overimposed to $E_{1/2}$. The experimental data were fitted to the $R_s Q_I$ (electrolyte A) and a $R_s Q_I R_I W_I$ (electrolyte B) equivalent circuits using the EcoChemie NOVA Frequency Response Analyzer (FRA) 1.8. The latter is a variation of the Randles circuit [24] (see Scheme S1†) which considers contributions from the electrolyte resistance (R_s), double-layer charging (constant phase element, Q_I), mass transport (Warburg impedance, W_I), and the apparent charge transfer resistance (R_I).

AFM images were acquired in tapping mode with a Nano-Observer microscope (CSI, Les Ulis, France). The surfaces were inspected using silicon cantilevers from AppNano (USA, Ref: ACT-50). The raw topographies were leveled and, then, the root-mean-square surface roughness (R_{MS}) and different height profiles were extracted using the freeware Gwyddion 2.56. FESEM was conducted in secondary electrons with a FEI Quanta 400FEG Genesis X4M Microscope with EDX Analysis (Centro de Materiais da Universidade do Porto, CEMUP). Graphene powder samples were investigated by

XPS and ATR-FTIR spectroscopy. XPS experiments were performed with a Kratos Axis Ultra HSA coupled to a 90 W achromatic Al ($K\alpha$) X-ray source and a Rowland circle monochromator of 500-mm (CEMUP). FTIR measurements were performed in a Bruker Tensor 27 spectrometer equipped with an ATR module (Bruker Corporation, USA).

2.3 Electrode Modification

A commercial GCE (Metrohm, 6.1204.300, area: 0.06 cm²) was mechanically polished to mirror finish using a 0.3 μ m Alumina slurry (Buehler Micropolish II), then, washed in UPW and ethanol in an ultrasonic bath (15 min each). To assess its cleanliness, CVs were registered in H₂SO₄ 0.5 M. Graphenes were deposited onto the surface of a freshly cleaned GCE using the drop-casting method. To this end, 10 μ L of GO (diluted in UPW to concentrations between 0.1 and 500.0 μ g·mL⁻¹) and rGO suspensions (dispersed in DMF within the same concentration range) were spread onto the GCE surface and allowed to air dry. Before use, the modified electrodes were washed with UPW and PBS and stored at 4 °C when not in use.

3. RESULTS AND DISCUSSION

3.1. Characterization of the Film Precursors

3.1.1 FTIR Spectroscopy

The chemical composition of GO and rGO was investigated by ATR-FTIR (Fig 1A). The spectrum of the former (solid black line) exhibits a broad band at 3300 cm⁻¹ (O-H stretching in hydroxyl groups and/or adsorbed water) and several sharper peaks. In good agreement with the literature [25,26], these have been assigned to: (a) symmetric C-O stretching vibration in carbonyl moieties (1730 cm⁻¹), (b) asymmetric O-C-O stretching in deprotonated carboxylic acids (1622 cm⁻¹), (c) C-O stretching in hydroxyl-substituted C atoms (1226 cm⁻¹), (d) epoxy C-O-C stretching (1049 cm⁻¹), and (e) asymmetric ring deformation in epoxides (976 cm⁻¹). The absence of these signals in the spectrum of rGO (red line) reflects the massive removal of oxygen-containing functional groups (O-groups). This result confirms that the commercial rGO presents a significantly lower degree of oxidation than its GO counterpart, which is consistent with the O-contents declared by the supplier (see Section 2.1).

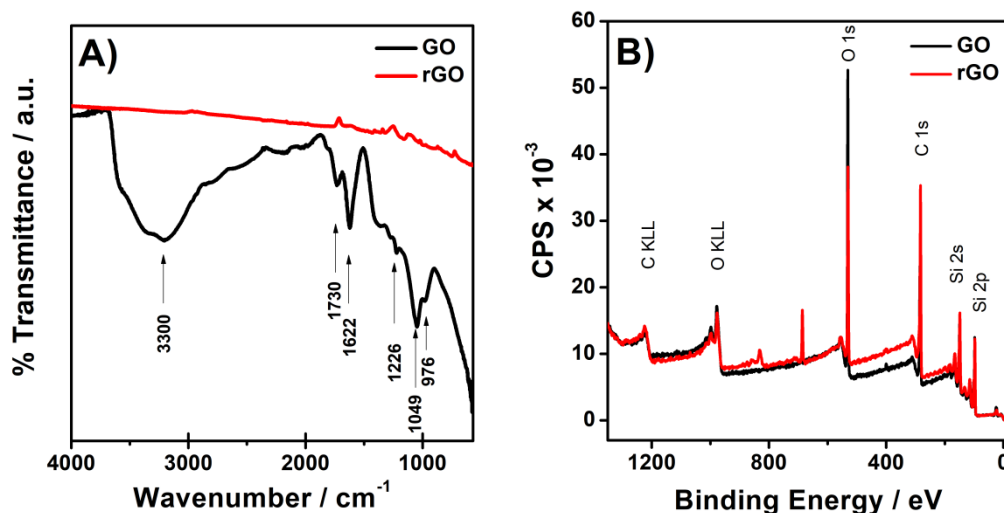


Figure 1. ATR-FTIR (A) and wide XPS (B) spectra recorded for the GO (black curve) and rGO powders (red).

3.1.2 XPS

The wide XPS spectra acquired for GO and rGO are compared in Fig 1B. For rGO, the O 1s peak (located at 531 eV) followed a significant decrease (with the I_{O1s}/I_{C1s} ratio falling from 2.1, GO, to 1.1). In good agreement with previous reports [26-29], the de-convoluted core C 1s spectrum of GO displays three bands (Fig S1A in the ESI†) at 285.0 (sp² hybridized C=C bonds), 287.1 (C-O bonds in hydroxyl residues and epoxy groups) and 288.9 eV (C-O bonds in carbonyl groups). The high ratio of intensities between the first two peaks ($I_{287}/I_{285}=1.21$) indicates the predominance of sp³ hybridized C atoms in the GO sheets. By de-convolution of the rGO spectrum (Fig S1B†), four peaks were found at: 285.0 (C=C), 285.9 (hydroxyl C-O), 287.3 (epoxy C-O), and 289.6 eV (C=O). Nevertheless, the peak intensities look completely different. While the C=C peak is twice as intense as found for GO, the C-O signals dropped dramatically. Consistent with the FTIR data, all these results confirm that the commercial rGO is a well-reduced product with a significantly restored network of the π -conjugated electrons.

3.2. Microscopic Characterization of Graphene Films

3.2.1 GCE/GO

Fig 2 shows a collection of cantilever deflection images (find the topographies in Figs S2 & S3†) obtained for the surface of a GCE before (panel 2A) and after modification with increasingly concentrated dispersions of GO (2B-2J). The former (blank or sample GO#0 in Table 1) exhibited a very smooth surface (as illustrated by the low R_{MS} of 5.5 nm) with deep linear scratches reflecting usage history. By increasing [GO], pronounced changes in the morphological appearance of the surfaces were triggered. In the range of 0.5-5.0 $\mu\text{g}\cdot\text{mL}^{-1}$ (Figs 2B-2D), bright particles are spotted over the glassy carbon, GC, surface (dark background).

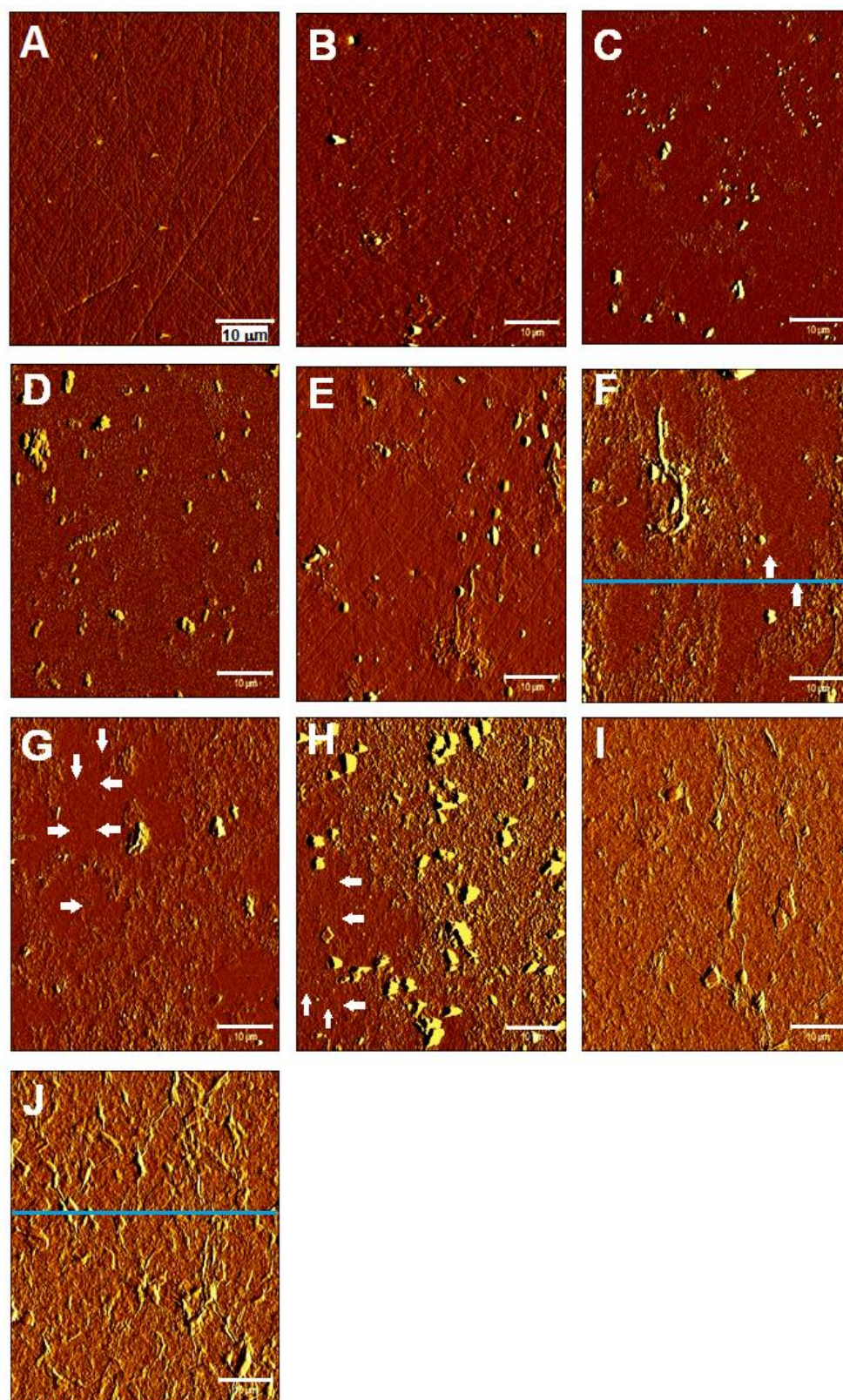


Figure 2. Amplitude $50\ \mu\text{m} \times 50\ \mu\text{m}$ AFM images registered in tapping mode for the surfaces of GCE/GO electrodes prepared from dispersions of the following concentrations: (B) 0.500, (C) 1.00, (D) 5.00, (E) 10.0, (F) 25.0, (G) 50.0, (H) 100, (I) 250, and (J) $500\ \mu\text{g}\cdot\text{mL}^{-1}$ GO. White arrows indicate the paths of surface scratches. Height profiles were extracted along the blue lines. The scale bar is $10\ \mu\text{m}$. The image obtained for the bare GCE (A) is also included for better comparison.

The amount and dimensions of these bodies rose slightly to a size of 3-4 μm at 5.0 $\mu\text{g}\cdot\text{mL}^{-1}$ (Fig 2D). In parallel, the R_{MS} increased steadily up to 37.5 nm (GO#3 in Table 1). Based on the high O-content unveiled in Section 3.1, the pK_a of carbonyl groups in GO (4.5-6.5) [30], and the physiological pH of the rinsing buffer (7.4); GO sheets should wear a negative net charge.

Table 1. Root-mean-square surface roughness (R_{MS}) measured for bare GCE, GCE/GO, and GCE/rGO electrodes from their corresponding topographic AFM images (Figs S3† in the ESI).

Sample	[GO] / $\mu\text{g}\cdot\text{mL}^{-1}$	R_{MS} / nm	[rGO] / $\mu\text{g}\cdot\text{mL}^{-1}$	R_{MS} / nm
#0	0.0	5.50	0.0	5.50
#1	0.5	7.80	0.5	6.30
#2	1.0	21.3	1.0	9.30
#3	5.0	37.5	5.0	10.8
#4	10.0	24.2	10.0	16.0
#5	25.0	55.5	25.0	16.1
#6	50.0	36.6	50.0	71.3
#7	100.0	44.9	100.0	84.2
#8	250.0	26.4	250.0	102.8
#9	500.0	50.0	500.0	187.1

Under such conditions, repulsive electrostatic interactions established between the neighbor sheets should outbalance the hydrophobic and π - π stacking forces that rule graphene aggregation. Therefore, the small particles found in this range can be ascribed to individual or very small aggregates of GO sheets. The scratches discussed above are still found in the backgrounds of Figs 2B-2E and, with more difficulties, in Figs 2F-2H (white arrows).

This observation proves that large areas of the original surface remain unmodified even for [GO] as high as 50 $\mu\text{g}\cdot\text{mL}^{-1}$. In the range 10-100 $\mu\text{g}\cdot\text{mL}^{-1}$ (Fig 2E-2H) the surface became increasingly covered with islands of wrinkled appearance and the R_{MS} oscillated between 24 and 55 nm. The latter finding suggests the concatenation of roughening-smoothing loops as the surface gets loaded with more material. A height profile was extracted along the blue line in panel 2F. As shown in Fig S5†, islands are relatively short (≈ 70 nm with peaks of 130 nm) and likely formed upon the agglomeration of individual GO sheets. At higher concentrations (Figs 2I & 2J), the islands coalesce into a relatively uniform, thick, and wrinkled film that coats the entire surface (surface scratches are no longer visible). In line with this finding, R_{MS} never surpassed its highest value (obtained at 25.0 $\mu\text{g}\cdot\text{mL}^{-1}$). The whole body of AFM evidence is consistent with a GCE surface that only gets fully covered at levels around 100 $\mu\text{g}\cdot\text{mL}^{-1}$.

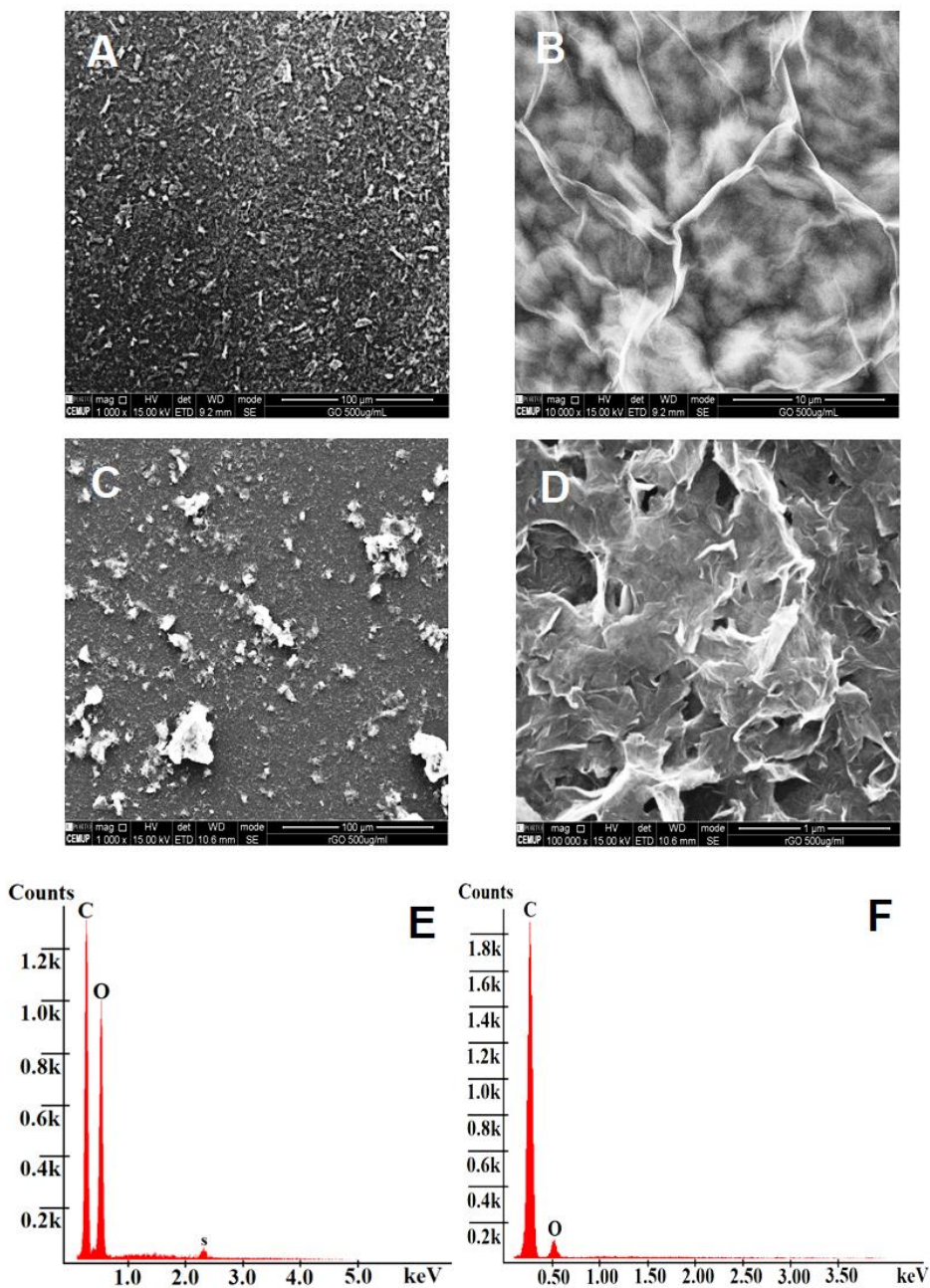


Figure 3. Top-view FESEM images taken for GCE/GO#9 (A) and GCE/rGO#9 electrodes (C) in secondary electrons with a 1,000 X magnification factor (MF). Panels B and D showcase a couple of regions of the previous images investigated in higher detail (MF= 10,000 X and 100,000 X, respectively). The EDX spectra taken at those locations are shown in panels E (GO) and F (rGO).

A second height profile was extracted for GO#9 (Fig S6†). The curve shows an internal structure that appears to consist of two incomplete layers (thickness: 78-74 nm each) settling on top of a complete base layer (≈ 70 nm).

Such a structure determines the wrinkled morphology observed under the scanning probe microscope. Accordingly, the brightest features in Figs 2I & 2J may represent the tallest regions of the multilayered film. GO#9 was further investigated by SEM (Fig 3A). In good agreement with Fig 2J, the image displays a surface uniformly covered with a densely packed, relatively homogeneous, and wrinkled film. The structure of its outermost layer was inspected in greater detail using a 10X higher magnification factor (MF). The zoomed image (Fig 3B) shows irregular, defect-free, and flat sheets of 10-15 μm with no signs of aggregation. As suggested by the height data Fig S6[†], sheets seem to stack on top of each other in a lying-down configuration (Scheme S2[†]). To investigate the elemental composition of the film, an EDX spectrum was taken at the same location (Fig 3E). The results showcased two intense peaks at 0.27 and 0.52 keV ascribed to C and O atoms, respectively. The counts ratio amounts to only 1.3 which illustrates the high O-content of GO (around 50%, according to the supplier).

3.2.2 GCE/rGO

The first relevant aspect is the observation of the surface scratches described in Section 3.2.1 in the background of all the images in Fig 4. Hence, in contrast with the full coverage achieved for $[\text{GO}] > 50 \mu\text{g}\cdot\text{mL}^{-1}$, it was never reached by rGO within the investigated range. Figs 4B & 4C resemble those discussed for GCE/GO in Figs 2B & 2C and show a nearly empty and scratchy GC surface decorated with small particles of 1-3 μm (isolated rGO sheets or small aggregates). In the range between 5 and 25 $\mu\text{g}\cdot\text{mL}^{-1}$, the density of surface particles overtakes the observed for their GO counterparts but no signs of island-type growth are detected in Figs 4E or 4F. The latter is further supported by the much smaller values of R_{MS} (16 nm vs the 55 nm measured for GO#5). The impact of aggregation phenomena became more evident for $[\text{rGO}] > 25 \mu\text{g}\cdot\text{mL}^{-1}$. In this regard, R_{MS} underwent a steep increase to 71 nm (rGO#6) and 103 nm (rGO#8). Unlike GO sheets, their reduced counterparts are expected to wear a much smaller net charge due to their lower O-content and that should translate into a higher impact of aggregation (just as observed in the images). It seems worth noting that R_{MS} values are not only much higher but also rose continuously with increasing $[\text{rGO}]$ (Fig S7B[†]).

Contrary to the roughening-smoothing mechanism leading to the assembly of well-packed GO films, rGO deposits as spherical aggregates of increasing size and coverage. Since no smoothing takes place, full coverage is never achieved and no uniform films are formed at any stage of the modification process. This can be better appreciated in Figs 4I & 4J, which display big holes that allow a glimpse of the scratchy surface of GC. In line with this view, R_{MS} grew continuously to a maximum of 187 nm. The SEM images captured for rGO#9 can be found in Figs 3C & 3D. In good agreement with Fig 4J, the former shows a distribution of large aggregates over a widely uncovered surface. As the region surveyed here is wider ($>200 \times 200 \mu\text{m}^2$), it can be inferred that the fraction of uncovered surface area is higher than suggested by the AFM data.

We examined the individual aggregates in more detail using a 102-fold higher MF (Fig 3D). As occurs with GO, the image unveils individual sheets that appear to stack on top of each other. Nevertheless, these feature noticeably less sharp edges and corners and look a lot more defective and

corrugated than GO sheets. This makes perfect sense if one considers that graphite oxide reduction methods introduce massive amounts of defects in the basal plane [31,32].

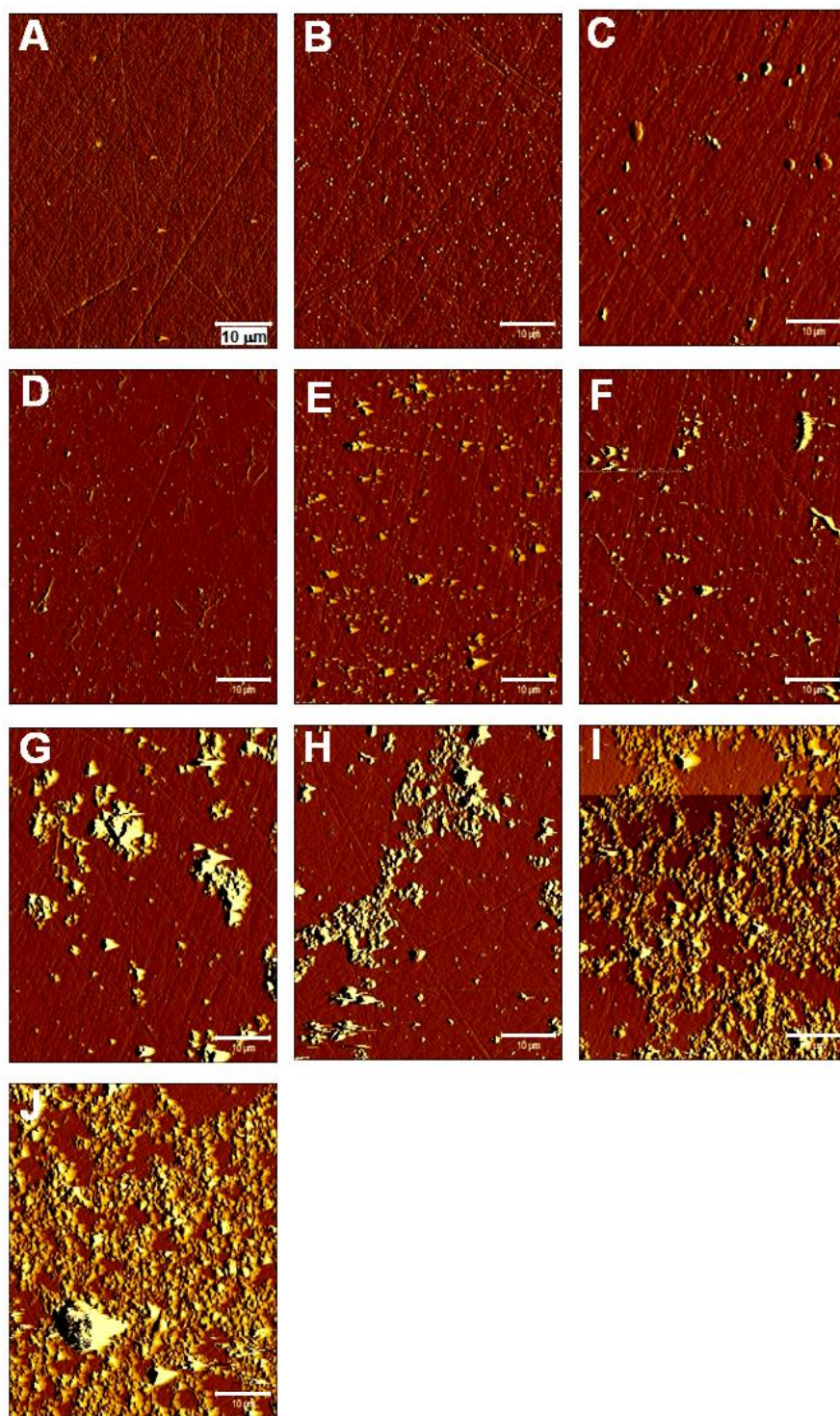


Figure 4. Amplitude $50\ \mu\text{m} \times 50\ \mu\text{m}$ AFM images registered in tapping mode for the surfaces of GCE/rGO electrodes prepared from dispersions of the following concentrations: **(B)** 0.500, **(C)** 1.00, **(D)** 5.00, **(E)** 10.0, **(F)** 25.0, **(G)** 50.0, **(H)** 100, **(I)** 250, and **(J)** $500\ \mu\text{g}\cdot\text{mL}^{-1}$ GO. The scale bar is $10\ \mu\text{m}$. The image obtained for the bare GCE **(A)** is also included for better comparison.

3.3. Electron Transfer Studies

3.3.1 GCE/GO

Fig 5 presents the CVs and impedance spectra measured for the GO-modified electrodes (colored solid curves) in electrolytes A and B. The voltammogram recorded for bare GCE (control or GO#0) in the former, displays a marked capacitive behavior with no distinctive Faradaic peaks (black dashed curve in panel A). Such behavior could have been anticipated since electrolyte A contains no redox species. The deposition of increasing amounts of GO did not change the shape of the CVs (colored curves).

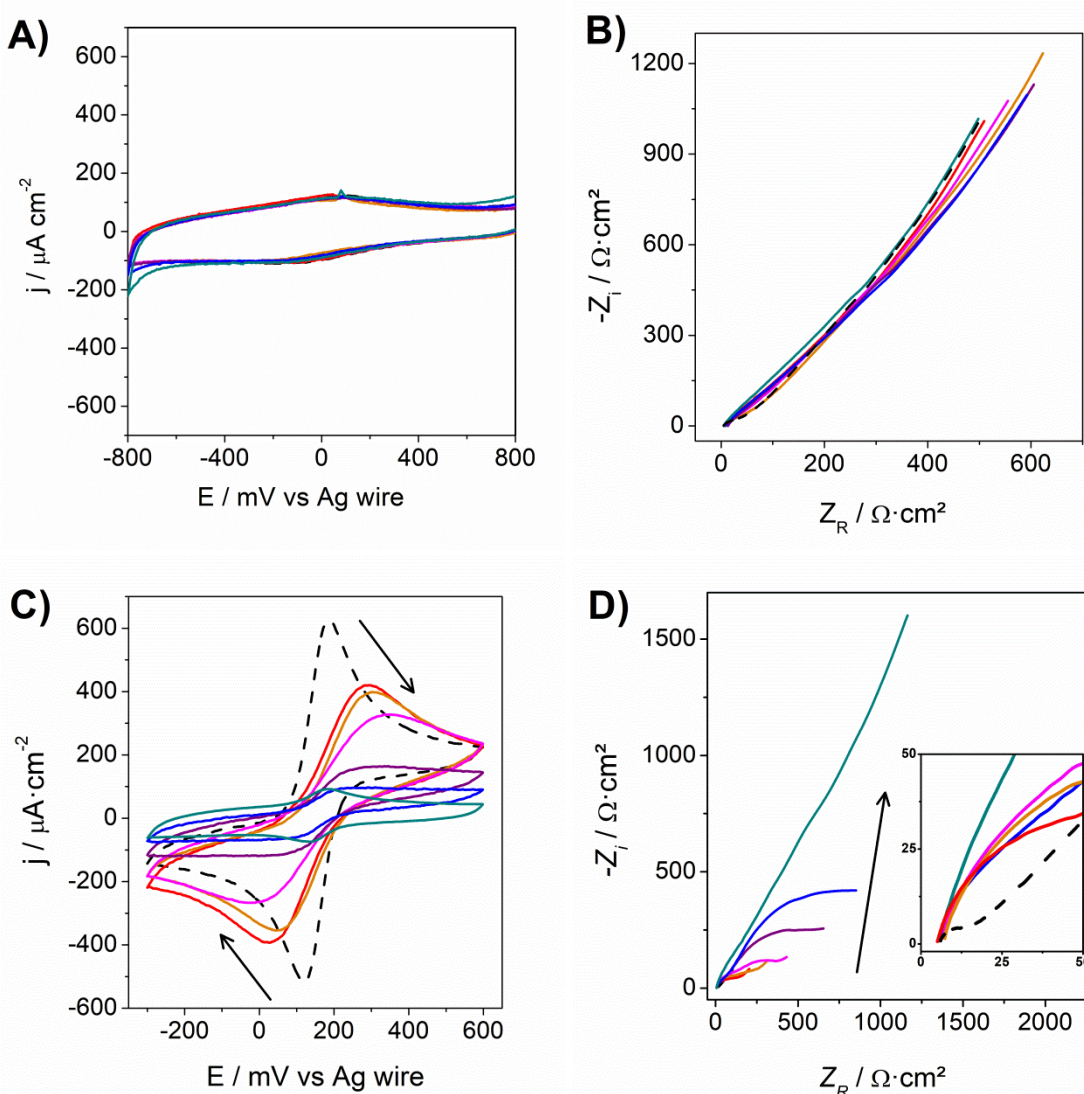


Figure 5. CVs (A, C) and Nyquist plots (B, D) recorded in PBS 0.05 M (A & B) and PBS 0.05 M + 2 mM $[\text{Fe}(\text{CN})_6]^{4-/3-}$ (C & D) for GCE/GO electrodes prepared from dispersions with $[\text{GO}]$: 0.5 (red solid line), 5.0 (orange), 10.0 (magenta), 50.0 (purple), 250.0 (blue), 500.0 $\mu\text{g}\cdot\text{mL}^{-1}$ (dark cyan). The blanks registered with the bare GCE (black dashed line) are included for comparison purposes. The inset in (D) shows in greater detail the shape of the spectra in the mid-high frequency range. In (A) & (C), ν was $0.05 \text{ V}\cdot\text{s}^{-1}$ in all cases. In (B) & (D), the spectra were taken at $+0.15 \text{ V}$ with an OA of 10 mV .

On the other hand, all the acquired Nyquist plots exhibit a linear response (panel B). It is worth emphasizing that the $-Z_i$ vs Z_R plot of a pure capacitor is typically characterized by a high-slope straight line as those observed in the figure [33]. Besides, the impedance spectra overlapped each other with no particular trend. These findings allow us to postulate that coating the GCE with GO does not produce any appreciable improvement in the double-layer capacitance in pure buffer (even for films as homogeneous as those in Figs 2J and 3A). The presence of 2 mM $[\text{Fe}(\text{CN})_6]^{3-/4-}$ provided deeper insights into the ET processes through the modified electrodes (panels C & D).

Table 2. Anodic peak current densities (j_{PA}), peak-to-peak potential difference (ΔE_P), and apparent charge transfer resistance (R_I) derived from the CVs and Nyquist plots recorded for the different GCE/GO electrodes in electrolyte B.

Sample	[GO] / $\mu\text{g}\cdot\text{mL}^{-1}$	j_{PA} / $\mu\text{A}\cdot\text{cm}^{-2}$	ΔE_P / mV	R_I / $k\Omega$
0.0	628	64	0.10	0.0
0.1	515	157	0.92	0.1
0.5	455	174	1.68	0.5
1.0	418	264	1.77	1.0
5.0	398	260	3.64	5.0
10.0	328	369	8.25	10.0
25.0	204	425	9.65	25.0
50.0	164	470	16.75	50.0
100.0	95	495	26.83	100.0
250.0	96	515	38.20	250.0
500.0	91	48	92.50	500.0

Table 2 summarizes the values of anodic peak current (j_{PA}), peak-to-peak potential difference (ΔE_P), and apparent resistance (R_I ; Section 2.2) measured for all the modified electrodes. The CV for GO#0 (dashed black curve in C) exhibits a pair of sharp Faradaic peaks separated by only 64 mV (close to the 59 mV theoretically expected for a fully reversible one-electron transfer at RT). As best seen in the inset of D, it also presents the smallest semicircle recorded at mid-high frequencies. Since this feature reflects the contribution of ET phenomena to the total impedance of the system, it is not surprising to find that it is closely related to the magnitude of R_I (the higher the ET resistance, the greater are both the magnitude of R_I and the semicircle diameter [34]). In line with this reasoning, GO#0 also scored the lowest R_I amongst all the investigated electrodes (101 Ω ; Table 2). The combination of very low ΔE_P and R_I confirm the fast ET kinetics of the $[\text{Fe}(\text{CN})_6]^{3-/4-}$ pair on GC. However, contrary to that found in the pure buffer, increasing the load of GO triggered dramatic changes in the shape of the CVs (colored solid lines).

From GO#0 to GO#9, the curves went progressively flat with j_{PA} falling from $628 \mu\text{A}\cdot\text{cm}^{-2}$ to $91 \mu\text{A}\cdot\text{cm}^{-2}$. Concomitantly, the peak separation grew up to $\Delta E_P=515$ mV. The semicircles in Fig 5D increased significantly and R_I followed an identical trend to reach 92.5 k Ω for GO#10. Unexpectedly, ΔE_P dropped below 59 mV for the latter. This finding would indicate a transition in the kinetics of the ET processes to a mixed regimen with major contributions of freely-diffusing and surface-confined probes. In any case, the ensemble of these results agrees with ET processes that become progressively hampered as the surface density of GO increases. This behavior is likely arising from the interplay between steric and electrostatic phenomena at the interface: (a) The adsorption of flaky micron-sized and electrically insulating GO sheets may block electroactive sites at the GC, thus, introducing hindrance for the probes to reach the electrode surface; (b) At the working pH, repulsive electrostatic forces must be established between the negatively charged redox probes and the abundant O-groups at GO. These phenomena would hinder the permeation of the films by the probes, thus, minimizing their concentration near the electrode surface.

As more GO is deposited, higher densities of physically blocked electroactive sites and O-groups available for electrostatic repulsion are expected to be found at the interface. Therefore, any increase in the coverage and thickness of the films would lead to a more pronounced blockage of the redox response (just as noticed in Figs 5C & 5D and Table 2). The effect of v was further explored for GO#2, GO#6, and GO#10. As shown in Fig S8†, the dependence of the peak potentials on v confirms that, in practical terms, the probes behave as quasi-reversible systems at the modified electrodes. Besides, j_{PA}/j_{PC} grew/decreased linearly with $v^{-1/2}$ in all cases. This behavior indicates that the response is kinetically controlled by the diffusion of the probes from the bulk electrolyte to the electrode surface and vice versa. The peak data was fitted to a couple of straight lines with the formula:

$$j_{PA/PC} = N + M_{A/C} \cdot v^{1/2} \quad (2)$$

The absolute values of the slopes ($|M_A|$ and $|M_C|$) declined by about five times from GO#0 to GO#10 (Table 3). This result confirms that the system is in a continuous departure from the ideal reversibility exhibited by GO#0 (something already suggested by the progressive increase of ΔE_P in Fig 5C and Table 2).

Table 3. Parameters obtained upon linear regression of the anodic and cathodic experimental data derived from Fig S8† to Eq. 2. For each sample, the slopes of the straight lines ($|M_A|$ & $|M_C|$, respectively) are presented together with the corresponding correlation coefficients (R^2). The diffusion coefficients (D_A & D_C), calculated from the slopes using Eq. 3, are also provided.

GO	$ M_A \cdot 10^{-4} /$ $\text{A}\cdot\text{cm}^2\cdot\text{s}^{1/2}\cdot\text{V}^{-1/2}$	$D_A \cdot 10^{-6} /$ $\text{cm}^2\cdot\text{s}^{-1}$	R^2	$ M_C \cdot 10^{-4} /$ $\text{A}\cdot\text{cm}^2\cdot\text{s}^{1/2}\cdot\text{V}^{-1/2}$	$D_C \cdot 10^{-6} /$ $\text{cm}^2\cdot\text{s}^{-1}$	R^2
#0	21.3	15.7	0.991	20.8	14.9	0.990
#2	16.9	9.89	0.998	15.4	8.18	0.996
#6	9.98	3.44	0.999	9.16	2.90	0.989
#10	4.71	0.77	0.995	3.97	0.54	0.996

The AFM images in Fig 2 show a GC surface that gets covered with islands that coalesce into a homogeneous film. Could the loss of reversibility evidenced for the probes in Fig S8† and Table 3 be linked to the slower diffusion of the probes across the GO-coated domains? To answer this question, we calculated the effective anodic and cathodic coefficients of diffusion (D_A & D_C) for the $[\text{Fe}(\text{CN})_6]^{4-}$ species. To this end, Eqs 1 and 2 were combined into:

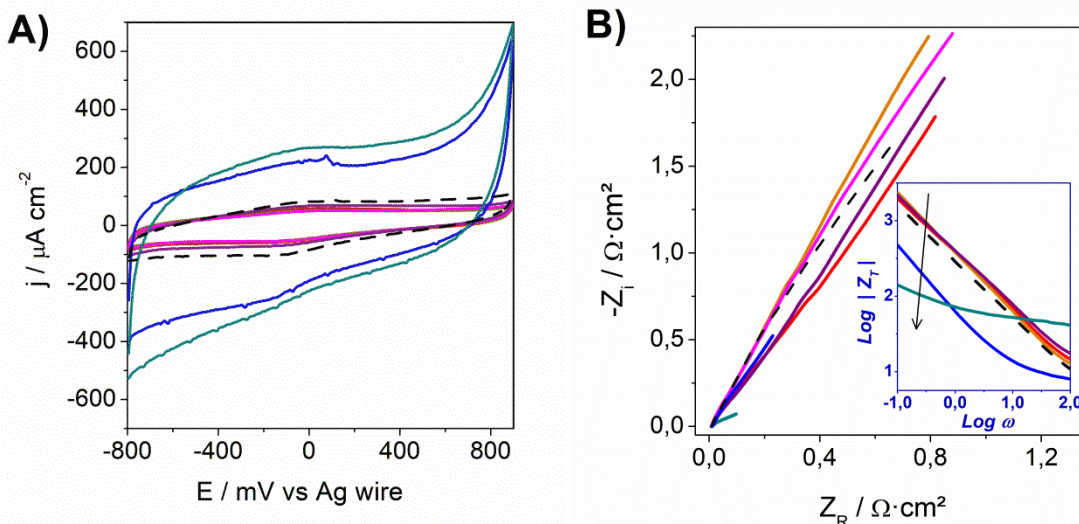
$$D_{AVC} = M_{AVC}^2 / (2.69 \cdot 10^5 \cdot C_{O/R})^2 \quad (3)$$

As shown in Table 3, the values for both coefficients dropped by almost two orders of magnitude from sample #0 to #10. This result confirms the progressive hindering of mass transport phenomena occurring in parallel with the rise in the coverage and thickness of the GO films.

3.3.2 GCE/rGO

Figs 6A shows some of the CVs recorded in electrolyte A. For [rGO] within the 0.1-100 $\mu\text{g}\cdot\text{mL}^{-1}$ range (RGO#1-RGO#8 in Table 4), the response was very similar to those by their GCE/GO counterparts and consist of purely capacitive currents with a magnitude close to those recorded with the blank (RGO#0). However, in sharp contrast to that seen in Fig 5A, double-layer currents increased dramatically for [rGO]>100 $\mu\text{g}\cdot\text{mL}^{-1}$ (especially for RGO#9 and RGO#11; blue and dark cyan curves in Fig 6A). Consistent with this behavior:

(a) The Nyquist plot recorded for the latter unveiled much lower values of $-Z_I$ and Z_R in the low-mid frequency (Fig 6B).



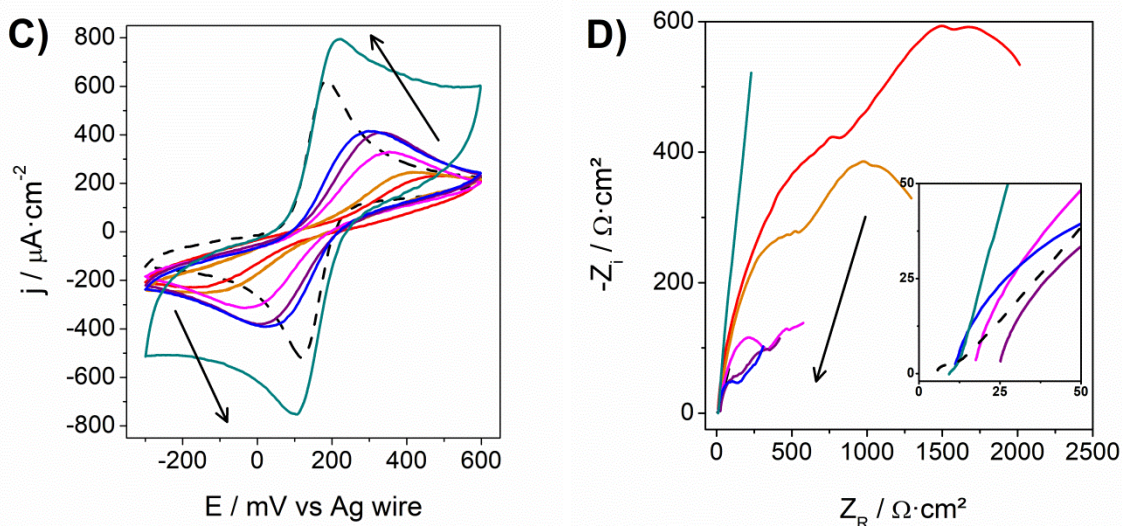


Figure 6. CVs (**A**, **C**) and Nyquist plots (**B**, **D**) recorded in PBS 0.05 M (**A** & **B**) and PBS 0.05 M + 2 mM $[\text{Fe}(\text{CN})_6]^{4-/3-}$ (**C** & **D**) for the GCE/rGO electrodes prepared from dispersions with $[\text{rGO}]$: 0.5 (red solid line), 5.0 (orange), 10.0 (magenta), 50.0 (purple), 250.0 (blue), and 500.0 $\mu\text{g}\cdot\text{mL}^{-1}$ (dark cyan). The curves registered with the bare GCE (black dashed line) are included for comparison purposes. The inset in (**D**) shows in greater detail the shape of the spectra in the mid-high frequency range. In (**A**) & (**C**), ν was $0.05 \text{ V}\cdot\text{s}^{-1}$ in all cases. In (**B**) & (**D**) the spectra were taken at $+0.15 \text{ V}$ with an OA of 10 mV .

(b) Their corresponding Bode plots (figure inset) confirm the significant decline of the total impedance (Z_T).

These shreds of evidence point towards a significant rise in the double-layer capacitance of the modified electrodes. This has been reported, indeed, to be one of the benefits commonly found for rGO-coated electrodes [35-37]. On the other hand, the electrochemical response in electrolyte B followed an opposite trend to that seen in Fig 5C and, instead of going flat, the CVs developed sharper and closer peaks together with a substantial increase of the double-layer currents (in good agreement with that seen in electrolyte A). Table 4 provides a quantitative view of the changes. RGO#11 reached the lowest ΔE_P in the series (103 mV) and peak currents that exceeded those measured with the blank ($j_{PA}=795$ vs $628 \mu\text{A}\cdot\text{cm}^{-2}$). The evolution of the Nyquist plots is shown in Fig 6D. Although for $[\text{rGO}] \leq 0.5 \mu\text{g}\cdot\text{mL}^{-1}$ (solid red curve) the semicircle region was substantially larger than that spotted for RGO#0 (figure inset), its rise above these values triggered a continuous drop in diameter. Accordingly, the smallest semicircle was registered by RGO#11 (even tinier than that of RGO#0). Interestingly, all the other spectra in the figure presented two overlapped semicircles. In line with this observation, Bode Phase plots also exhibited two waves (find the one for RGO#2 in Fig S11A†).

This particularity indicates that two independent ET processes, defined by different time constants, are taking place simultaneously at the interface. The AFM and SEM evidence showed that rGO fails to coat the entire surface of GC even at the highest concentrations explored. Hence, we assign each semicircle to the contributions of the electroactive sites located at rGO-coated and bare GC surface domains. Under this hypothesis, the single semicircle spotted for RGO#11 would indicate that

its response is completely dominated by one type of site (most likely the rGO-coated sites). Then, we fitted its impedance spectrum to the Randles-type circuit described in Section 2.2. Two time-constant systems are better represented by equivalent circuits with the ability to split contributions in non-arbitrary ways. To accomplish that, the experimental data for samples #1-#10 were successfully fitted to the two branches equivalent circuit depicted in Fig S11B†. This model has been previously applied in the literature to fit systems with an analogous type of impedimetric response [38,39]. In good agreement with the qualitative analysis of the spectra, the values of R_1 and R_2 derived from the fittings increased from RGO#0 to RGO#2 (to values of 10.4 and 31.7 k Ω , respectively).

At higher concentrations, R_1 declined by approximately two orders of magnitude to 0.13 k Ω (RGO#11), and R_2 even turned non-measurable for [rGO]>400 $\mu\text{g}\cdot\text{mL}^{-1}$. The latter behavior points to an important drop in the fraction of bare GC sites available for charge transfer. The effect of ν in the response of RGO#2, RGO#6, and RGO#11, was further explored (Fig S9†). In all cases, j_{PA} and j_{PC} exhibited linear dependence on $\nu^{-1/2}$ what indicates that the process is diffusion-controlled (as also found for GCE/GO). The magnitude of $|M_{AC}|$ declined by about half from RGO#0 to RGO#2. This is in line with the more hindered CV and EIS responses evidenced from Figs 6C & 6D. However, as opposed to the behavior of GCE/GO, rising [rGO] over 0.5 $\mu\text{g}\cdot\text{mL}^{-1}$ promoted a continuous enhancement in the reversibility of the system. This is supported by the rise in the slope of the j_{PA} vs $\nu^{-1/2}$ plots (insets of Figs S9A-S9C†) and the 1-fold increase followed by $|M_{AC}|$ and D_{AC} (Table 5). In good agreement, all the parameters derived for RGO#11 topped those obtained with the blank (e.g. D_{AC} were more than twice). Such a remarkable rise in the diffusion coefficients must necessarily point to a notable enhancement of the mass transport phenomena. The results are interpreted as follows:

A) 0-0.5 $\mu\text{g}\cdot\text{mL}^{-1}$. The significant increase of ΔE_p and R_1 plus the concomitant decrease of j_{PA} and D_{AC} indicates that the deposition of very low amounts of rGO on the GCE is enough to pose serious difficulties to the redox processes (compared to RGO#0). The low coverage reached from those dispersions (Fig 4B) suggests that these difficulties must emerge from a partial blockage of the electroactive sites at the GC surface by adsorption of individual, or slightly aggregated, rGO sheets (most likely in lying-down configuration; Scheme S2†). The great exposure of inert basal plane sites (compared to the more catalytic perimeter edge-sites [18,20-22]) occurring under this configuration, would also contribute to the more hindered response.

B) 0.5-500 $\mu\text{g}\cdot\text{mL}^{-1}$. The complete set of electrochemical data confirms that increasing the load of rGO results in a progressive enhancement of the electroactivity (to the point of exceeding the performance of the blank). Such a boost must stem from vast improvements in the double-layer capacitance and charge transfer kinetics.

In particular, the defective nature of the rGO sheets (with irregular perimeter lines and big holes within the basal plane) and the clustered aspect of the films (as discussed in Section 3.2) allow us to postulate that higher fractions of defective and edge sites must become available for charge transfer as [rGO] is increased. Recent studies have confirmed the correlation between the defect density and the electrocatalytic activity towards different electrochemical processes [40]. Besides, it cannot be discarded that the sheets could transition from the lying-down to sandwiched or standing-up phases in some particular clusters (Scheme S2†). Under the latter configuration, the sheets stack together perpendicularly to the surface plane and the ET processes would benefit from a greater exposure of

catalytic sites and from the restored in-plane electrical conductivity of the rGO sheets [16, 17] (thus, wiring more effectively the underlying GC surface to the ET reaction sites [41]). In this line, vertically-aligned assemblies of graphene sheets have recently demonstrated an enhanced sensitivity towards the detection of microcystin LR in tap water [42].

Aiming to understand the behavior at higher levels of rGO, we prepared two electrodes at 600 and 800 $\mu\text{g}\cdot\text{mL}^{-1}$ (RGO #12 & RGO#13, respectively). Their AFM images (Figs S4A & S4B†) revealed larger loads of deposited material but full coverage was never reached. Therefore, we can claim that no continuous rGO film is formed at any stage of the investigated modification. The CVs and Nyquist plots in Figs S10A & S10B†, showed a change in the trend observed up to 500 $\mu\text{g}\cdot\text{mL}^{-1}$: i.e. j_{PA} decreased from 795 (#11) to 481 $\mu\text{A}\cdot\text{cm}^{-2}$ (#13) and ΔE_P grew up to 124 mV (Table 4). Parallel to these changes, the size of the semicircles increased markedly and, in full agreement, R_f climbed to 51.1 k Ω . These results indicate that the electrochemical response declines over 500 $\mu\text{g}\cdot\text{mL}^{-1}$. As the films grow in size and thickness, more rGO sheets are expected to pile onto each other leading to the progressively blocking of the internal structure of the film to the electrolyte species. That may explain the net decrease in the electroactivity noticed in Fig S10†. Therefore, for $[\text{rGO}] > 500 \mu\text{g}\cdot\text{mL}^{-1}$, these phenomena (i.e. steric hindrance and the obstruction of mass transport phenomena) would outbalance the benefits of the greater densities of catalytic sites.

4. CONCLUSIONS

We have assembled films of GO and rGO from liquid dispersions in a wide range of concentrations. The microscopic evidence gathered for the former, revealed relatively thin and uniform films of wrinkled morphology formed upon stacking of freestanding, large-area, and mostly defect-free sheets of GO (with almost negligible impact of aggregation) in roughening-smoothing cycles. In striking contrast, the more defective and corrugated rGO sheets deposit in the form of clusters of increasing size (no smoothing). These particularities determine that while full coverage is quickly achieved for concentrations of GO above 50.0 $\mu\text{g}\cdot\text{mL}^{-1}$, this simply does not occur for $[\text{rGO}]$ as high as 800 $\mu\text{g}\cdot\text{mL}^{-1}$. These differences in structure and morphology have been correlated, for the first time, to the electrochemical response of the modified electrodes. The compact and uniform films formed by electrically insulating GO not only do not improve the double-layer capacitance of the bare GCE but hinder the charge transfer processes of reversible probes. On the other hand, rGO induced a significant boost in capacitance for concentrations above 250 $\mu\text{g}\cdot\text{mL}^{-1}$ and consistently enhanced the charge transfer processes in the range 0.05-500 $\mu\text{g}\cdot\text{mL}^{-1}$. At higher levels, the increase in electroactive area (with greater exposure of catalytic edge and basal-defect sites) is outbalanced by the mass transport difficulties induced by the thicker and more compact rGO stacks. Thus, the best electroactivity was reached at 500 $\mu\text{g}\cdot\text{mL}^{-1}$. These results are not only critical to better understand some of the discrepancies found in the literature but are also key to build a more rational design of nanostructured multilayered films with GNMs at their base.

AUTHOR CONTRIBUTIONS

Following CRediT standards: P.M.V.F. played a major role in the investigation, validation, and visualization. J.M.C. contributed to conceptualization, methodology, visualization, supervision, project administration, funding acquisition, and writing. C. M. P. and A.F.S. played contributions in conceptualization, supervision, resources, and funding acquisition.

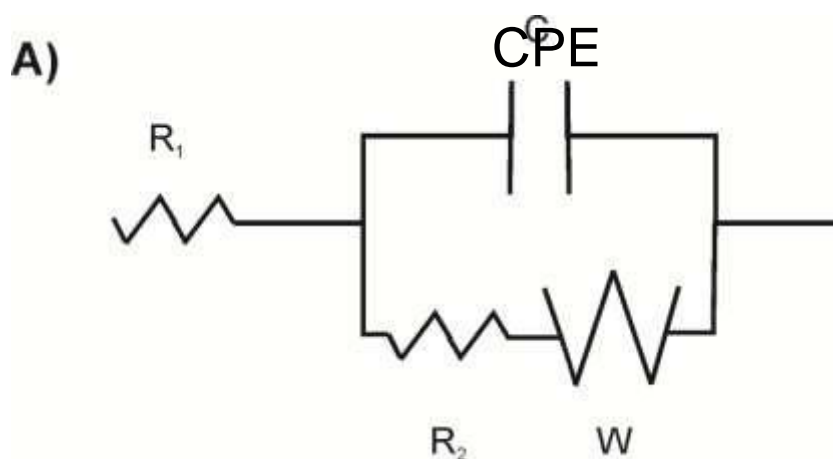
ACKNOWLEDGMENTS

This work was supported by European (FEDER) and Portuguese regional funds (NORTE2020 program) through projects Pest-C/EQB/LA0006/2013 and NORTE-01-0145-031968 (RapidPhageSensing). P.M.V.F. acknowledges the Fundação para a Ciência e a Tecnologia de Portugal (FCT) for the concession of a doctoral grant (SFRH/BD/111274/2015).

SUPPLEMENTARY DATA:

A. Randles-type Equivalent Circuits

The variation of the Randles circuit [1] used in this work is referred to as R_1QR_2W (see an schematic representation after this paragraph). Instead of the typical capacitor in the Randles circuit, here we include a Constant Phase Element (CPE or Q) which accounts for the topological imperfections of the electrode surface. R_1 is the electrolyte resistance, R_2 is the charge transfer resistance, and W is the Warburg diffusion impedance. When the charge transfer is the rate determining step (for instance, for the GCE/GOx electrode), the Warburg element can be neglected and the system is electrically equivalent to a R_1QR_2 circuit.



Scheme S1 – Randles-type circuit used to fit the data acquired in electrolyte B.

B. Supplementary Results

B. 1 XPS Data

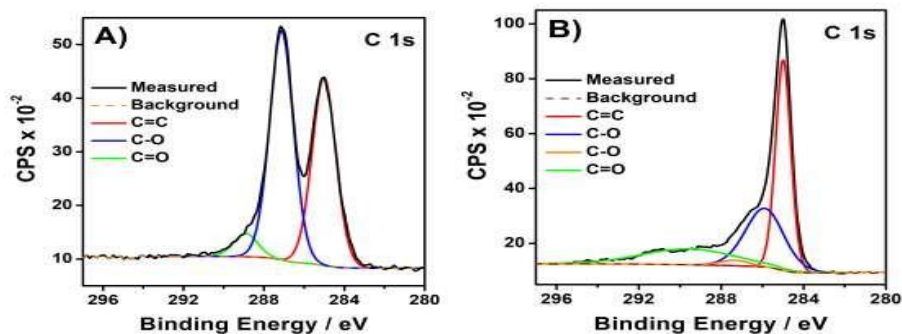


Figure S1 - C 1s core spectra (black solid curves) taken for GO (A) and rGO powders (B) and their corresponding de-convoluted peaks (colored curves).

B. 2 AFM

B.2.1

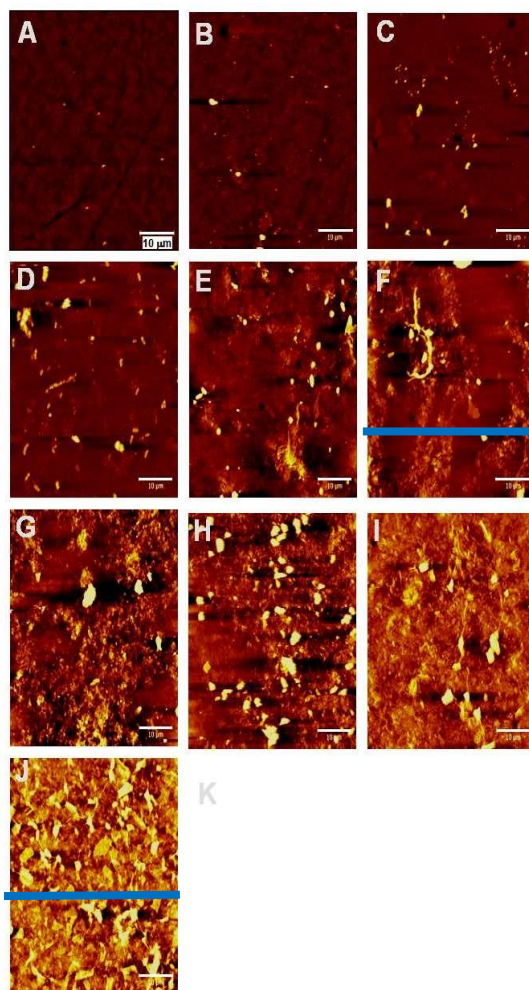


Figure S2 – AFM 50 x 50 μm topographies taken for the GCE/GO electrodes modified with dispersions of the following [GO]: (B) 0.500, (C) 1.00, (D) 5.00, (E) 10.0, (F) 25.0, (G) 50.0, (H) 100, (I) 250, and (J) 500 μg·mL⁻¹ GO. The scale bars are 10 μm. Bare GCE is shown in (A) for better comparison.

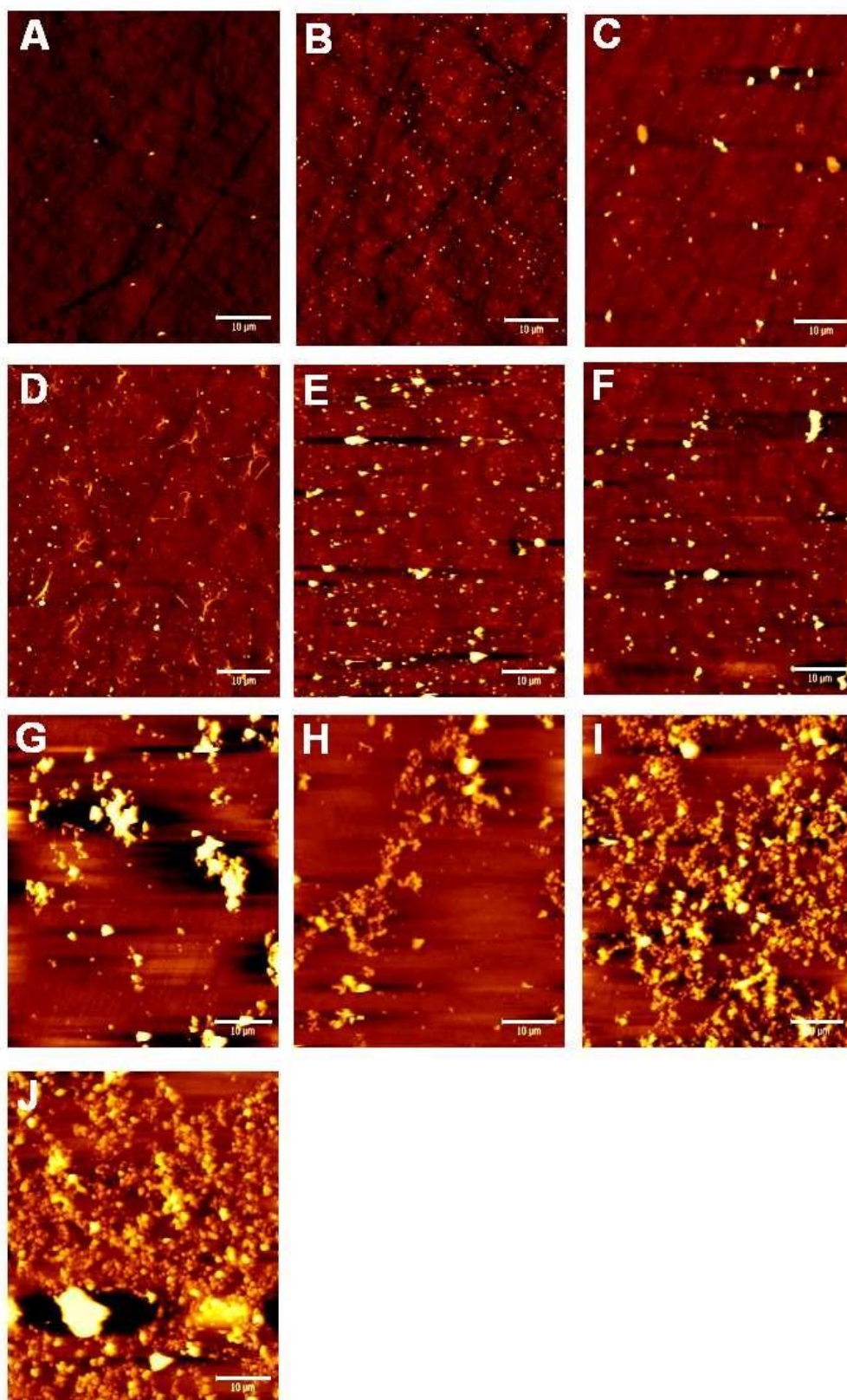


Figure S3 – AFM 50 x 50 μm topographies taken for the GCE/rGO electrodes modified with dispersions of the following [rGO]: **(B)** 0.500, **(C)** 1.00, **(D)** 5.00, **(E)** 10.0, **(F)** 25.0, **(G)** 50.0, **(H)** 100, **(I)** 250, and **(J)** 500 $\mu\text{g}\cdot\text{mL}^{-1}$ rGO. The scale bars are 10 μm . Bare GCE is shown in **(A)** for better comparison.

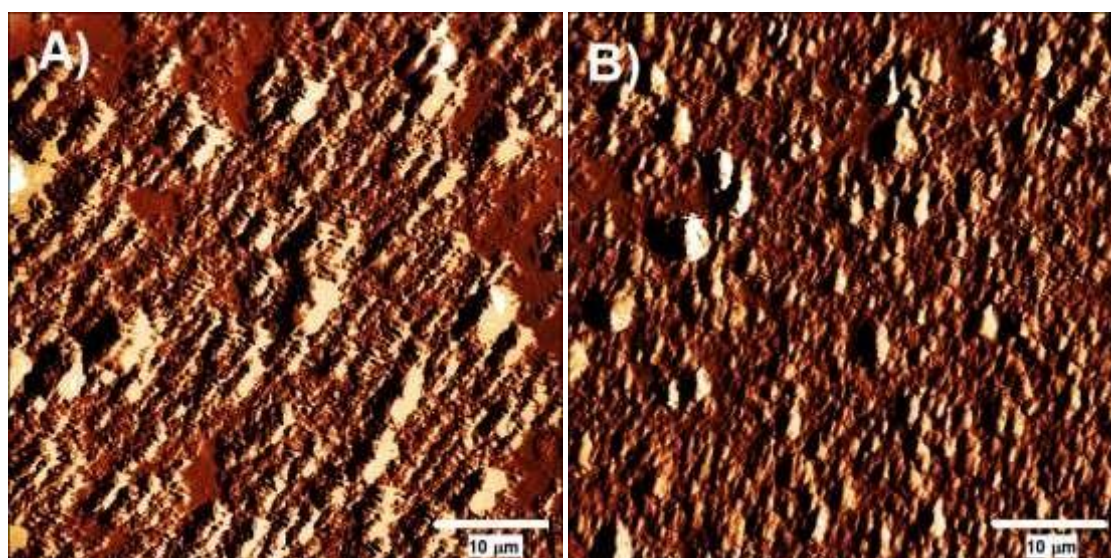


Figure S4 – AFM 50 x 50 μm topographies taken for GCE/rGO electrodes prepared upon dropcasting of dispersions with [rGO]: (A) 600, and (B) 800 $\mu\text{g}\cdot\text{mL}^{-1}$ rGO.

B.2.2 Height Profiles

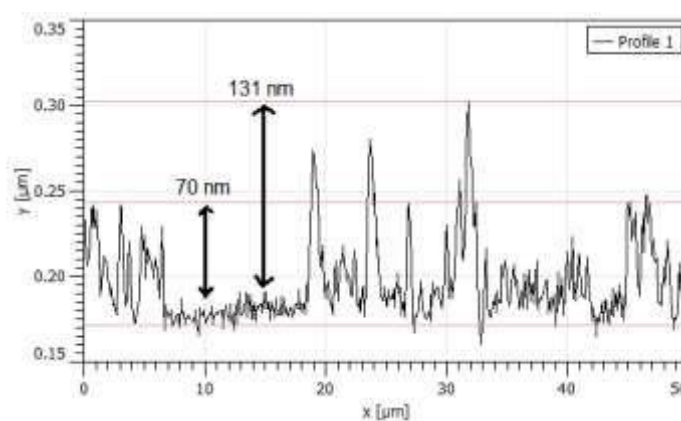


Figure S5 – Height profile extracted along the blue line in Fig S2F.

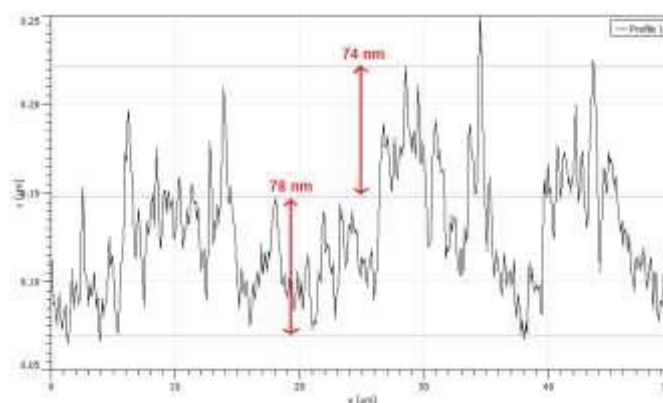


Figure S6 – Height profile extracted along the blue line in Fig S2J.

B.2.3 R_{MS} vs. Graphene Concentration Plots

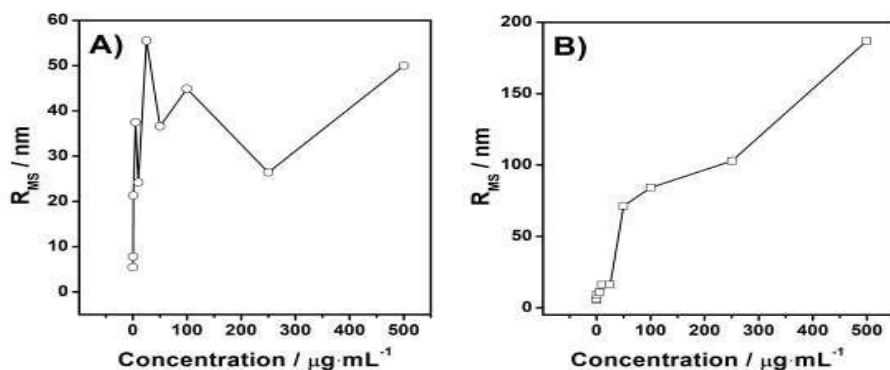


Figure S7 – Evolution of R_{MS} plots for GCE/GO (A) and GCE/rGO electrodes (B).

B. 3 Scan Rate Effect

B.3.1 GCE/GO Electrodes

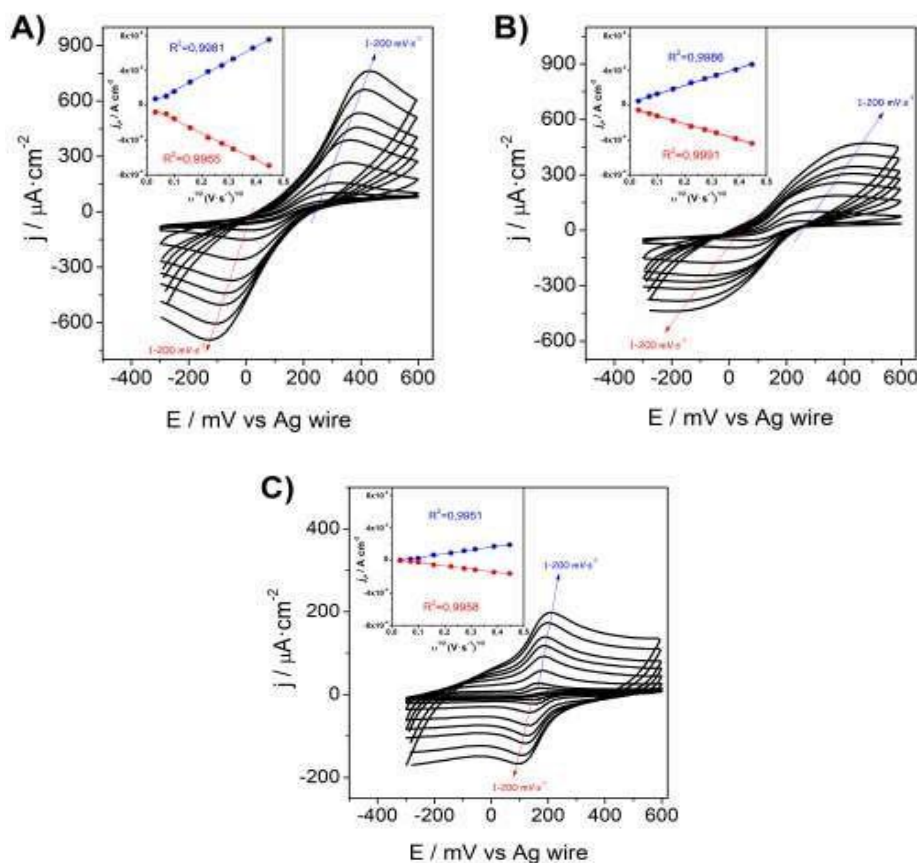


Figure S8 – CVs consecutively registered for electrodes GO#2 (A), GO#6 (B), and GO#10 (C), by increasing the scan rate (\square) in the range $1-200 \text{ mV}\cdot\text{s}^{-1}$. The insets show the evolution of the anodic (blue full circles) and cathodic (red) peak current densities (j_p) vs. $\square^{1/2}$. The least squares fitting lines of the data are also included (solid lines) together with the corresponding correlation coefficients (R^2). The electrolyte was PBS 0.05 M (pH 7.4) + 2 mM $[\text{Fe}(\text{CN})_6]^{4-/3-}$ in all cases.

B.3.2 GCE/rGO Electrodes

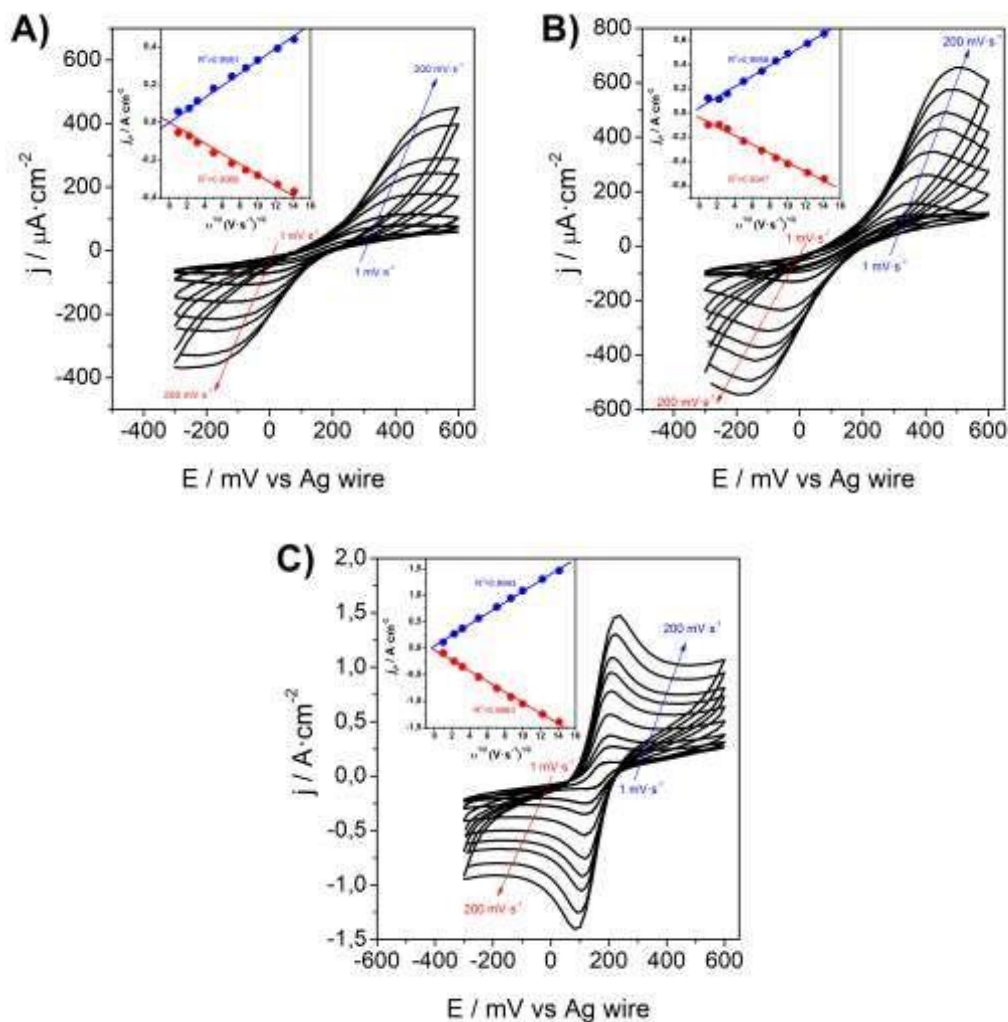


Figure S9 – CVs consecutively registered for rGO#2 (A), rGO#6 (B), and rGO#11 (C), by increasing the scan rate (\square) in the range 1-200 $\text{mV}\cdot\text{s}^{-1}$. The insets show the evolution of the anodic (blue full circles) and cathodic (red) peak current densities (j_p) vs. $\square^{1/2}$. The fitting lines are also included (solid lines) with the corresponding correlation coefficients (R^2). The electrolyte was PBS 0.05 M (pH 7.4) + 2 mM $[\text{Fe}(\text{CN})_6]^{4-/3-}$ in all cases.

B. 4 Electrodes RGO#12 & RGO#13

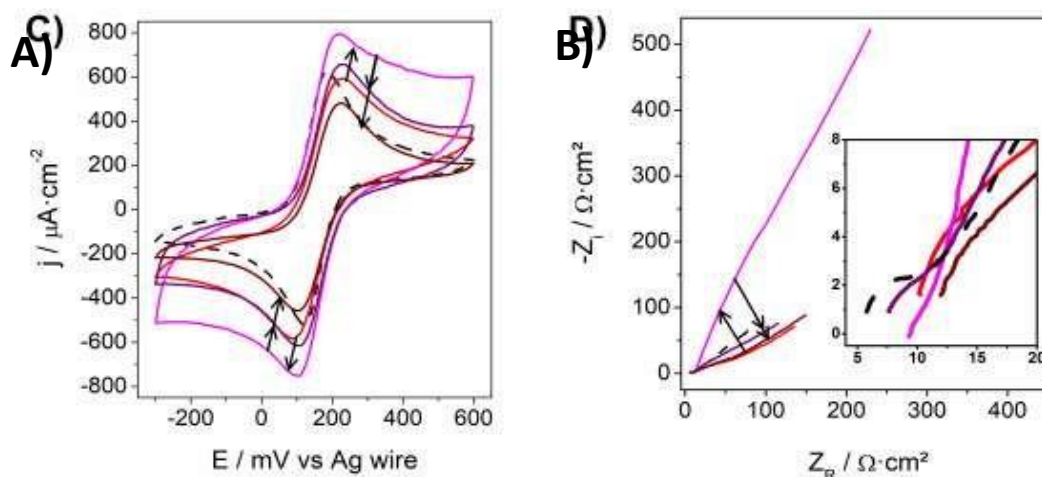


Figure S10 – CVs (A) and Nyquist plots (B) registered in PBS 0.05 M + 2 mM $[\text{Fe}(\text{CN})_6]^{4/3-}$ for GCE/rGO electrodes prepared with $[\text{rGO}] = 400$ (red solid line), 500 (magenta), 600 (purple), and 800.0 $\mu\text{g}/\text{mL}$ (wine). The curves recorded for the bare GCE (black dashed line) are included for comparison purposes.

B. 5 EIS Data

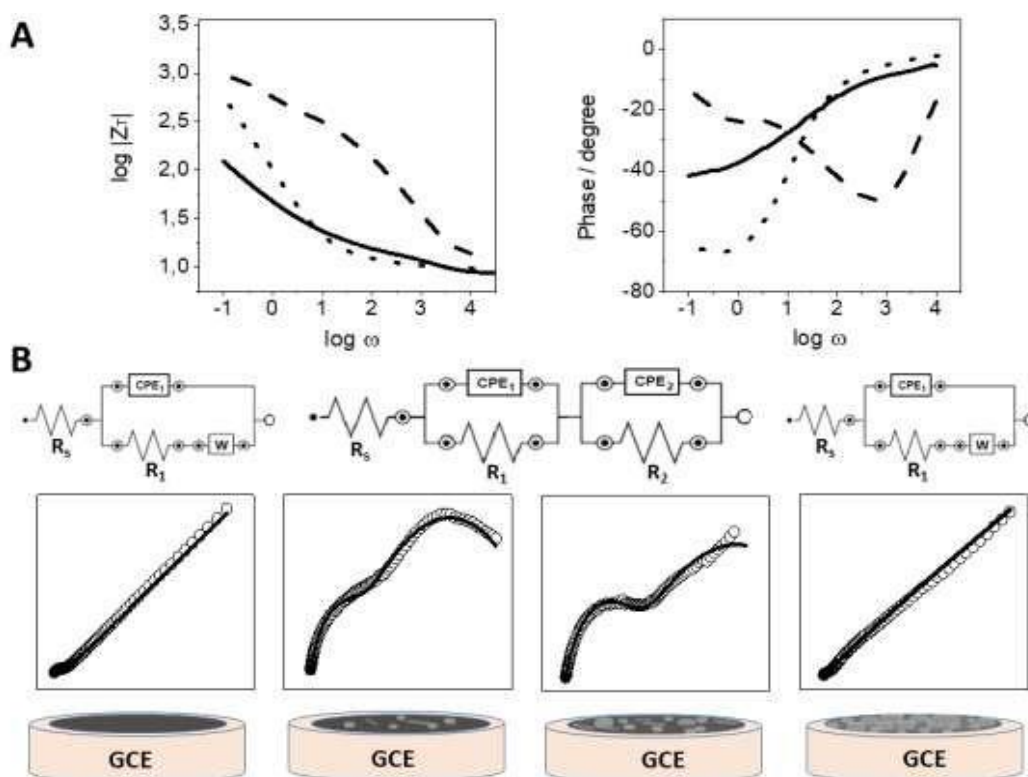


Figure S11 – A) Bode (left) and Bode Phase (right) plots acquired for RGO#0 (solid line), RGO#2 (dashed line), and RGO#11 (dotted line). B) Correlations between the recorded Nyquist plot (from left to right: RGO#0, RGO#2, RGO#8, and RGO#11), the equivalent circuits used for data fitting, and the morphological aspect of the electrode surface (as reconstructed from the microscopic evidence in Figs 2-4) in each case. The black solid lines in the plots represent the fitted spectra.

C. Packing Configuration



Scheme S2 – Art model illustrating different packing configurations for graphene sheets (GO or rGO) on solid surfaces.

References

1. J. E. B. Randles, Kinetics of Rapid Electrode Reactions, *Discuss. Faraday Soc.* 1947, 1, 11-19.
2. G. Bharath, R. Madhu, S-M. Chen, V. Veermani, A. Balamurugan, D. Mangalaraj, N. Ponpandian, Enzymatic Electrochemical Glucose Biosensors by Mesoporous 1D Hydroxyapatite-on-2D Reduced Graphene Oxide, *J. Mater. Chem. B* 2015, 3, 13601370

References

1. K. S. Novoselov, A. K. Geim, S. V. Morozov, D. Jiang, Y. Zhang, S. V. Dubonos, I. V. Grigorieva and A. A. Firsov, *Science*, 306 (2004) 666.
2. Y. B. Zhang, Y. W. Tan, H. L. Stormer, and P. Kim, *Nature*, 438 (2005) 201.
3. X. Y. Fang, X. X. Yu, H. -M. Zheng, H. -B. Jin, L. Wang and M. -S. Cao, *Phys. Lett. A*, 379 (2015) 2245.
4. T. J. Davies, M. E. Hyde, and R. G. Compton, *Angew. Chem. Int. Ed.*, 44 (2005) 5121.
5. P. Rani and V. K. Jindal, *RSC Adv.*, 3 (2013) 802.
6. M. Pumera, *Mater. Today*, 14 (2011) 308.
7. T. Turcheniuk, R. Boukherrou, and S. Szunerits, *J Mater Chem B*, 3 (2015) 4301.
8. Z. Lu, S. Li, C. Liu, C. He, X. Yang, D. Ma, G. Xu and Z. Yang, *RSC Adv.*, 7 (2017) 20398.
9. E. Yoo, J. Kim, E. Hosono, H. S. Zhou, T. Kudo and I. Honma, *Nano Lett.*, 8 (2008) 2277.
10. C. Liu, Z. Yu, D. Neff, A. Zhamu and B. Z. Jang, *Nano Lett.*, 10 (2010), 4863.
11. F. Yu, C. Wang and J. Ma, *Materials*, 9 (2016) 807.
12. Z. Y. Yin, J. X. Zhu, Q. Y. He, X. H. Cao, C. L. Tan, H. Y. Chen, Q. Y. Yan and H. Zhang, *Adv. Energy Mater.*, 4 (2014) 1300574.

13. S. H. Huh, In: S. Mikhailov (Ed.), *Physics and Applications of Graphene – Experiments*, InTech Open, 2011, 73-90.
14. X. Feng, W. Chen and L. Yan, *RSC Adv.*, 6 (2016) 80106.
15. M. Acik, G. Lee, C. Mattevi, M. Chhowalla, K. Cho and Y. J. Chabal, *Nat. Mater.*, 9 (2010) 840.
16. Y. Yang, A. M. Asiri, Z. Tang, D. Du and Y. Lin, *Mater. Today*, 16 (2013) 365.
17. M. Zhou, Y. Zhai and S. Dong, *Anal. Chem.*, 81 (2009) 5603.
18. D. A. C. Brownson, L. J. Munro, D. K. Kampouris and C. E. Banks, *RSC Adv.*, 1 (2011) 978.
19. M. S. Goh and M. Pumera, *Anal. Chem.*, 82 (2010) 8367.
20. D. K. Kampouris and C. E. Banks, *Chem. Comm.*, 46 (2010) 8986.
21. P. M. Hallan and C. E. Banks, *Electrochem. Comm.*, 13 (2011) 8.
22. S. J. Rowley-Neale, D. A. C. Brownson and C. E. Banks, *Nanoscale*, 8 (2016) 15241.
23. F. Chekin, A. Vasilescu, R. Jijie, S. K. Singh, S. Kurungot, M. Iancu, G. Badea, R. Boukherroub and S. Szunerits, *Sens. Actuators B Chem.*, 262 (2018) 180.
24. J. E. B. Randles, *Discuss. Faraday Soc.*, 1 (1947) 11.
25. M. Ciszewski, A. Mianowski, P. Szatkowski, G. Nawrat, and J. Adamek, *Ionics*, 21 (2014) 557.
26. C. Hu, Y. Liu, Y. Yang, J. Cui, Z. Huang, Y. Wang, L. Yang, H. Wang, Y. Xiao and J. Rong, *J. Mater. Chem. B*, 1 (2013) 39.
27. F. Tuz Johra and W.-G. Jung, *Appl. Surf. Sci.*, 357 (2015) 1911.
28. J. Riga, J. Pireaux, R. Caudano and J. J. Verbibst, *Phys. Scr.*, 16 (1977) 346.
29. H. Estrade-Szwarckopf, *Carbon*, 42 (2004) 1713.
30. T. Serodre, N. A. P. Oliveira, D. R. Miquita, M. P. Ferreira, A. P. Santos, V. G. Rsende and C. A. Furtado, *J. Braz. Chem. Soc.*, 30 (2019) 2488.
31. Y. H. Wu, T. Yu and Z. X. Shen, *J. Appl. Phys.*, 108 (2010) 071301.
32. S. J. Park and R. S. Ruoff, *Nat. Nanotechnol.*, 4 (2009) 217.
33. J. R. MacDonald, *Impedance Spectroscopy*, Wiley (1987), New York, USA.
34. J. M. Campiña, A. Martins and F. Silva, *J. Phys. Chem. C*, 111 (2007) 5351.
35. F. Tuz Johra and W-G. Jung, *Appl. Surf. Sci.*, 357 (2015) 1911.
36. D. Govindarajan, V. U. Shankar and R. Gopalakrishnan, *J. Mater. Sci.: Mater. Electron.*, 30 (2019) 16142.
37. F. Meng, L. Zhao, Y. Zhang, J. Zhai, Y. Li and W. Zhang, *Ceram. Int.*, 17 (2019) 23701.
38. L. Wang, J. Zhao, X. He, J. Gao, J. Li, C. Wan and C. Jiang, *Int. J. of Electrochem. Sci.*, 7 (2012) 345.
39. B. E. McNealy and J. L. Hertz, *Solid State Ion.*, 256 (2014) 52.
40. R. Ashwini, Z. Mohanta, M. K. Punith Kumar, M. S. Santosh, and C. Srivastava, *Carbon Trends* 5 (2021) 100095.
41. N. M. Sanches, A. Hassan, I. A. Mattioli, L. J. A. Macedo, G. C. Sedenho, F. N. Crespilho, *Adv. Mater. Interfaces*, 8 (2021) 2100550.
42. L. Wang, W. Zhang, S. Samavat, D. Deganello, and K. S. Teng, *ACS Appl. Mater. Interfaces*, 12 (2020) 35328-35336.